

# Experimental Validation of Optimized Solar Cell Capacitance Simulation for Rheology-Modulated Carbon-Based Hole Transport Layer-Free Perovskite Solar Cell

Sreeram Valsalakumar,\* Shubhranshu Bhandari,\* Tapas K. Mallick, Justin Hinshelwood, and Senthilarasu Sundaram

The hole transport layer (HTL)-free carbon-based perovskite solar cell (C-PSC) has attracted the attention of researchers due to its ease of fabrication and reduced costs in the manufacturing process. The rheological and physical characteristics of the solutions influence the layer quality of different device fabrication methods. Herein, the HTL-free structure of C-PSC through solar cell capacitance simulator (SCAPS) simulations is analyzed and validated with experimental results using rheology-varied mesoporous-TiO<sub>2</sub> (m-TiO<sub>2</sub>) paste. Regarding the m-TiO<sub>2</sub> rheology, two different samples (Type 1 and Type 2) are used, and six different configurations by thickness variation are analyzed utilizing SCAPS simulations. For Type 1 and Type 2, the best configurations exhibit theoretical efficiencies of 16.40% and 16.81%, respectively, without the influence of the resistance factor. After replicating similar designs in experiments, the efficiencies become 10.12% and 12.20%, respectively. Further, results are investigated by SCAPS simulations incorporating series and shunt resistance values, resulting in efficiencies of 10.56% and 12.59% for Type 1 and Type 2, respectively, which is comparable with actual devices. Finally, the variation of theoretical and experimental results is scrutinized with the help of impedance spectroscopy and external quantum efficiency, demonstrating the significance of this work for commercialization aspects.

low-cost manufacturing options have drawn the attention of various researchers, making it one of the most emerging photovoltaic (PV) technologies.<sup>[7–10]</sup> Improvements in PSC have led to an efficiency of 26.1%, which can be compared to the current commercially available PV technology.<sup>[11]</sup> While most of the highly efficient lab-based PSCs include a hole transport layer (HTL) and an expensive metal electrode, this hinders the commercialization process due to higher manufacturing costs.<sup>[12,13]</sup> To overcome these difficulties, tremendous efforts have been made in the development of HTL-free carbon-based PSC (C-PSC).<sup>[14]</sup> The HTL-free architecture simplifies the fabrication process, and the carbon electrode makes perovskite devices more stable compared to other metal electrodes.<sup>[15]</sup> In 2013, Ku et al. demonstrated the first C-PSC with an efficiency of 6.6%, followed by, in 2014, Anyi et al. demonstrated the HTL-free C-PSC with a PCE of 12.8% and stability of more than 1000 h in ambient light conditions.<sup>[16,17]</sup>

After several years of efforts, the highest reported efficiency for C-PSC is 20.04%, which is still higher than 16% efficiency of HTL-free C-PSC.<sup>[18–21]</sup>

The mesoporous scaffold structure (TiO<sub>2</sub>/ZrO<sub>2</sub>/perovskite) is the most commonly used for C-PSC fabrication, and it helps enhance the perovskite/carbon interface connection.<sup>[22,23]</sup>

## 1. Introduction

Within a decade, perovskite solar cells (PSCs) have become a promising technology for harnessing solar energy.<sup>[1–6]</sup> Advancements in power conversion efficiency (PCE), optoelectronic tunability, and

S. Valsalakumar, S. Bhandari, T. K. Mallick  
Environment and Sustainability Institute  
University of Exeter  
Penryn Campus, Cornwall TR10 9FE, UK  
E-mail: sv353@exeter.ac.uk; s.bhandari@exeter.ac.uk

 The ORCID identification number(s) for the author(s) of this article can be found under <https://doi.org/10.1002/aesr.202300244>.

© 2024 The Authors. Advanced Energy and Sustainability Research published by Wiley-VCH GmbH. This is an open access article under the terms of the Creative Commons Attribution License, which permits use, distribution and reproduction in any medium, provided the original work is properly cited.

DOI: 10.1002/aesr.202300244

J. Hinshelwood  
College of Engineering, Mathematics and Physical Science  
University of Exeter  
Penryn Campus, Cornwall TR10 9FE, UK

S. Sundaram  
School of Computing, Engineering and Design Technologies  
Teesside University  
Tees Valley, Middlesbrough TS1 3BX, UK

The annealing temperature during the fabrication of C-PSC with scaffold structure is (usually in the range of 400–500 °C) higher compared to most of the planar PSC structures with metal electrodes.<sup>[24,25]</sup> Even though the need for a higher temperature during the fabrication increases the cost, the carbon electrode's inherent stability acts as a moisture protective layer due to the hydrophobic nature of different carbon materials and vast possibilities for engineering the electrode to induce the hole transport materials.<sup>[16,26]</sup> Moreover, the compatibility of carbon electrode coating with the halide perovskite material and the simple fabrication process accelerated research work in the HTL-free C-PSC field.<sup>[27]</sup> In 2012, Lioz Etgar et al. reported the first HTL-free CH<sub>3</sub>NH<sub>3</sub>PbI<sub>3</sub>/TiO<sub>2</sub>-based C-PSC with a PCE of 7.3%.<sup>[28]</sup> Various efforts have been made to engineer the carbon electrode to overcome the poor mechanical interface connection between carbon/perovskite.<sup>[28,29]</sup> More recently, in 2023, Siqi Li et al. reported a flexible HTL-free C-PSC by incorporating the carbon nanotubes to enhance the interface connection between the perovskite and carbon, achieving a PCE of 14.44%.<sup>[28]</sup>

Additionally, in the commercialization aspect of the C-PSC, the fabrication mechanisms are crucial for determining the cell or the panel characteristics, especially for large-scale fabrication processes such as slot-die coating, screen printing, inkjet printing, spray coating, and blade coating.<sup>[18,30,31]</sup> The layer quality and the parameters depend on the rheological properties of the ink.<sup>[32]</sup> The rheology influences key characteristics such as leveling, vertical flow, and adhesion, which collectively affect the thin-film coating process.<sup>[32,33]</sup> Moreover, the shrinkage and pressure on the coating mechanism will vary with respect to the rheology of the solution.<sup>[33,34]</sup> As a whole, the layer thickness changes, and eventually, that will affect the bandgap of the thin film.<sup>[32]</sup> Since solution-processed C-PSC is also classified as a thin-film emerging PV, the rheological balancing of the material improves the reproducibility and enhances the translation rate of high-performance lab scale devices to the industrial level.<sup>[35,36]</sup> Various researches reveal the influence of absorber layer thickness on cell performance.<sup>[37]</sup> As the absorber layer thickness increases, longer-wavelength illumination spectra generate more electron–hole pairs.<sup>[38]</sup> In contrast, reducing the absorber thickness results in closer contact between the back electrode and the depletion layer, attracting more electrons for recombination.<sup>[38]</sup> Both the absorber layer thickness and the variation in the bandgap due to the electron transport layer (ETL) thickness have a considerable effect on the PV performance.<sup>[37]</sup> In this respect, theoretical analysis can be combined with experimental possibilities, where solar cell capacitance simulator (SCAPS)-1D simulation has a significant influence. Depending on different perovskite device structures and a wide range of materials, SCAPS-1D simulation can predict the maximum PCE for a device, analyzed through mathematical interpretations.

In this work, we simulated the performance of different HTL-free C-PSC with the SCAPS-1D software and validated the results with the experimental data. For the study, the ETL layer rheology data were taken from our previous work and used for the simulation and cell fabrication.<sup>[39]</sup> Based on the comparison of both experimental and simulated data, we analyzed the effect of rheological balancing and its influence on the film properties. In order to understand performance variation, the configuration with the highest performance in the SCAPS simulation was

replicated through the experiment and analyzed using various measurement studies.

## 2. Experimental Section

### 2.1. SCAPS Simulation

The numerical simulation of HTL-free C-PSC was conducted using the SCAPS-1D software program developed by researchers at the University of Gent.<sup>[40]</sup> The program analyzes the physical parameters of different layers and validates them with the proposed C-PSC structure. Solving the Poisson equation (Equation (1)), electron and hole continuity equation (Equation (2) and (3), respectively) provides C-PSC characteristics such as current density–voltage (*J–V*) and quantum efficiency. As shown in Equation (1), the Poisson equation provides the relation between the p–n junction electric field (*E*) and the volume charge density ( $\rho$ ).<sup>[41,42]</sup> Here,  $\epsilon$ ,  $q$ ,  $\psi$ ,  $n$ ,  $p$ ,  $N_d^+$ ,  $N_a^-$  represent permittivity, electron charge, electrostatic potential, total electron density, total hole density, and ionized donor and acceptor doping concentration, respectively.<sup>[41,42]</sup>

$$\frac{d}{dx} \left( -\epsilon(x) \frac{d\psi}{dx} \right) = q[p(x) - n(x) + N_d^+(x) - N_a^-(x)] \quad (1)$$

In the electron and hole continuity equation, Equation (2) and (3),  $j_n$ ,  $j_p$ ,  $R_n$ ,  $R_p$  denote electron density, hole density, electrons net recombination rate per volume, holes net recombination rate per unit volume, and the generation rate per unit volume, respectively.<sup>[42]</sup>

$$\frac{\partial j_n}{\partial x} = q \left( R_n - G + \frac{\partial n}{\partial t} \right) \quad (2)$$

$$\frac{\partial j_p}{\partial x} = -q \left( R_p - G + \frac{\partial p}{\partial t} \right) \quad (3)$$

In this work, planar n–i–p structure (FTO/TiO<sub>2</sub>/ZrO<sub>2</sub>/Perovskite/Carbon) was used, and the device parameters are listed in **Table 1**. The simulations were carried out under one sun illumination (AM1.5G, 100 mW cm<sup>-2</sup>) at 300-K and in the dark. The parameters for the active layer, ETL, and the defect layer, such as permittivity, density, thermal velocity, electron affinity, and mobility, were obtained from other literature.<sup>[20,27]</sup> The thickness and the optical bandgap for the ETL and active layers were obtained from the experimental data. To account for interface recombination in the PSC, ZrO<sub>2</sub> with a lower thickness was added between ETL and perovskite layers. The interface defects between the ETL/ZrO<sub>2</sub> and ZrO<sub>2</sub>/perovskite were considered neutral and single. In the SCAPS simulation, the interface defects between the ETL/ZrO<sub>2</sub> and ZrO<sub>2</sub>/perovskite layers were considered neutral, which implied they did not introduce a net charge or did not cause an excess of electrons or holes in the material.<sup>[37,38]</sup> Since the influence of ETL and perovskite layers in the C-PSC performance is mostly highlighted in this work, interface defects were made neutral and single for the uniformity of simulation results. Also, according to literature, the assumption of neutral and single defects facilitates a clearer understanding of the specific impact of ETL and perovskite layers'

**Table 1.** C-PSC layer's characteristic data used for the SCAPS software simulation.

Properties	ZrO <sub>2</sub>	Perovskite	TiO <sub>2</sub>
Thickness [nm]	120	Varied according to the configurations	Varied according to the configurations
Bandgap [eV]	3.75 <sup>[59]</sup>	1.56 <sup>[60]</sup>	Varied according to the configurations
Affinity [eV]	2.1 <sup>[59]</sup>	3.90 <sup>[61]</sup>	4.2 <sup>[27]</sup>
Dielectric Permittivity	10.7 <sup>[59]</sup>	10 <sup>[61]</sup>	10 <sup>[27]</sup>
DOS <sub>CB</sub> [cm <sup>-3</sup> ]	2.8 × 10 <sup>19</sup> <sup>[35]</sup>	2.76 × 10 <sup>18</sup> <sup>[62]</sup>	2.5 × 10 <sup>18</sup> <sup>[27]</sup>
DOS <sub>VB</sub> [cm <sup>-3</sup> ]	1.8 × 10 <sup>19</sup> <sup>[35]</sup>	3.9 × 10 <sup>18</sup> <sup>[62]</sup>	1 × 10 <sup>18</sup> <sup>[27]</sup>
μ <sub>e</sub> [cm <sup>2</sup> Vs <sup>-1</sup> ]	12 <sup>[59]</sup>	15 <sup>[63]</sup>	0.1 <sup>[27]</sup>
μ <sub>h</sub> [cm <sup>2</sup> Vs <sup>-1</sup> ]	25 <sup>[59]</sup>	15 <sup>[63]</sup>	0.1 <sup>[27]</sup>
Acceptor Concentration [cm <sup>-3</sup> ]	1 × 10 <sup>15</sup> <sup>[59]</sup>	1 × 10 <sup>11</sup> <sup>[20]</sup>	0 <sup>[27]</sup>
Donor Concentration [cm <sup>-3</sup> ]	0 <sup>[59]</sup>	0 <sup>[20]</sup>	1 × 10 <sup>19</sup> <sup>[27]</sup>

characteristics rather than complex arrangements.<sup>[37,38,42]</sup> Additionally, the work functions of carbon and FTO electrodes were 5.2 and 4.4 eV, respectively.

In this work, two types of m-TiO<sub>2</sub> pastes were used, one with lower viscosity (termed as Type 1) and the other with higher viscosity (termed as Type 2). The Type 1 and Type 2 pastes had viscosities of 2.85 cP and 3.85 cP, respectively.<sup>[39]</sup> The preparation method for the m-TiO<sub>2</sub> pastes was adopted from our previous report.<sup>[39]</sup> During the C-PSC fabrication, different rotation speeds for these Type 1 and Type 2 pastes provided various bandgaps for the m-TiO<sub>2</sub> layer. The SCAPS simulation parameters were adjusted accordingly, and three configurations were derived from each Type 1 and Type 2, as mentioned in Table 1 and 2. After analyzing various configurations, the ones that exhibited better performance from both Type 1 and Type 2 were selected for the C-PSC fabrication.

## 2.2. Device Fabrication

FTO-coated glass (2 cm × 2 cm) with a sheet resistance of 9–10 Ω sq<sup>-1</sup> was used for both Type 1 and Type 2 cell fabrications. The glass sheets were etched with the diluted hydrochloric acid and Zn powder, followed by an ultrasonic bath with detergent, distilled water, ethanol, and acetone for 20 min. Next, the samples underwent an ozone–ultraviolet treatment for 30 min. After the standard cleaning procedure, a blocking TiO<sub>2</sub> layer was deposited on the glass sheets using the spin coater at 5000 rpm for 60 s. The coated samples were placed on a hotplate and annealed at 500 °C for 30 min. Once cooled down to room temperature, the devices

were separated into two batches. One batch was coated with the lower viscous m-TiO<sub>2</sub> at 2000 rpm for 60 s using the spin coater and termed as Type 1. The other batch, termed Type 2, was coated with the higher viscous m-TiO<sub>2</sub> under the same condition. Both the samples were then annealed at 500 °C for 30 min and gradually cooled down to room temperature.

Next, a mesoporous ZrO<sub>2</sub> layer was coated on both batches at 4000 rpm for 30 s and annealed at 500 °C for 30 min. The ZrO<sub>2</sub> paste (1:5 ethanol diluted) was purchased from Solarnix. Finally, a mesoscopic carbon layer was coated over the samples using screen printing and annealed again at 450 °C for 30 min. Once it reached room temperature, an adequate amount of perovskite solution infiltrated through the carbon layer by drop casting and spin coating for 10 s at 1000 rpm. The samples were then annealed at 50 °C for 1 h, and all these processes were carried out under ambient conditions. The ion-exchange method was used for preparing perovskite solution, where 0.191 g MAI (Methyl ammonium iodide), 0.553 gm PbI<sub>2</sub>, and 0.015 g 5-aminovaleic acid iodide (5-AVAI) was mixed in 1 mL γ-butyrolactone (GBL) and heated at 70 °C for 30 min, followed by cooling. A filtration technique (0.2-micron PTFE) was used to remove the sediments. Finally, the measurements and characterizations for Type 1 and Type were carried out, and the C-PSC performance was recorded.

## 2.3. Characterization Techniques

The X-ray diffraction (XRD) study of the perovskite was conducted on the X'pert pro-MPD XRD of PANalytical with Cu

**Table 2.** Different SCAPS simulation configurations and experiment results for type 1.

No	Perovskite thickness [nm]	m-TiO <sub>2</sub> thickness [nm]	Rotation speed for m-TiO <sub>2</sub> layer [rpm]	m-TiO <sub>2</sub> bandgap [eV]	Simulation results	Efficiency [%]	V <sub>oc</sub> [V]	J <sub>sc</sub> [mA cm <sup>-2</sup> ]	FF
Sample 1	300	150	4000	3.2		13.11	0.795	20.36	80.90
Sample 2	450	300	3000	3.4		15.18	0.818	22.96	80.73
Sample 3	600	450	2000	3.5		16.40	0.839	24.275	80.52
Results									
Type 1 with sample 3 configuration	Series resistance (R <sub>s</sub> ) [Ω]	R <sub>CT</sub> [Ω]	R <sub>rec</sub> [Ω]	Efficiency [%]	V <sub>oc</sub> [V]	J <sub>sc</sub> [mA cm <sup>-2</sup> ]	FF		
	18.6	40	922	10.12	0.835	18.8	64.50		

$\text{K}\alpha$  radiation ( $\lambda = 1.5406 \text{ \AA}$ ). The scanning electron microscopy (SEM) (LEO 430i, Carl Zeiss) was used for the cross-sectional thickness analysis of the C-PSC devices. The C-PSC device testing was carried out under the illumination of  $1000 \text{ W m}^{-2}$  irradiation through a Wacom AAA continuous solar simulator (model: WXS-210S-20, AM 1.5 G) and the  $I$ - $V$  characteristics recorded with the EKO MP-160 I-V Tracer. For electrochemical impedance spectroscopy (EIS) study, AUTOLAB PGSTAT 10 with AUTOLAB frequency analyzer and frequency response analyzer module with a frequency range from 1 MHz to 0.1 Hz at  $V_{oc}$  (open-circuit voltage) was used. The experimental data fitting was carried out using the Z-view software (3.4d version, Scribner Associates, Inc., USA). The incident photon-to-current density (IPCE) and external quantum efficiency (EQE) were measured through the BENTHAM PVE300 equipment with the condition of 350–750 nm wavelength by a tungsten halogen lamp source.

### 3. Results and Discussion

#### 3.1. Simulation Parameters and Structural Analysis

In the present study, HTL-free C-PSC was used for the SCAPS simulation with a configuration of FTO/TiO<sub>2</sub>/ZrO<sub>2</sub>/perovskite/carbon, as shown in **Figure 1A**. Here, the TiO<sub>2</sub> acts as an ETL layer and the carbon is the back contact electrode. In addition, the parameters like bandgap, thickness, electron mobility, and other characteristics for the simulation are depicted in Table 1. Here,  $\text{DOS}_{CB}$  and  $\text{DOS}_{VB}$  are the acceptor and donor density, respectively, and  $\mu_e$  and  $\mu_h$  are the electron mobility and hole mobility.<sup>[27]</sup>

The chemical analysis of the 5-AVAI-based perovskite was performed by XRD, and **Figure 1B** indicates the crystalline nature.

The major peaks at  $\approx 14^\circ$ ,  $24.4^\circ$ ,  $28.4^\circ$ , and  $31.8^\circ$  equivalent to (110), (111), (201), and (211) planes confirm the crystalline perovskite.<sup>[43,44]</sup> The cross-sectional SEM illustrated in **Figure 1C,D** differentiates the nature of the layer nature and the configuration of the C-PSCs. The varied thicknesses of the layers are visible in **Figure 1C** for type 1 and **1(D)** for type 2 C-PSCs. Since the cells are fabricated through the perovskite infiltration technique, the entire perovskite thickness is taken as the sum of the carbon, ZrO<sub>2</sub>, and m-TiO<sub>2</sub> layers for SCAPS simulation. Even though the thickness difference of perovskite and m-TiO<sub>2</sub> in both Type 1 and Type 2 is comparatively less, cell performance variations were identified during the simulation and experiment study. Nevertheless, in the simulation, only the perovskite thickness across the ZrO<sub>2</sub> and m-TiO<sub>2</sub> was taken into account. However, the SCAPS simulation method is unable to perform the study of C-PSCs fabricated with the perovskite infiltration technique. Moreover, the thickness of the perovskite alongside both bandgap and thickness of the m-TiO<sub>2</sub> layers were varied according to each configuration in the Type 1 and Type 2 samples.

#### 3.2. Factors Influencing SCAPS Simulation

The performance of the C-PSC significantly depends on the perovskite absorption film, as the light absorption by the photo-generated carriers increases in the absorber layer.<sup>[45]</sup> During the simulation studies, the quality of the perovskite layer was influenced by defect density and the average experimental value was between  $10^{14}$  and  $10^{16} \text{ cm}^{-3}$ .<sup>[36]</sup> A higher defect density in the perovskite absorber layer reduces the C-PSC performance. In the fabrication setup, low-quality perovskite film enhances the defect density, which dominates carrier recombination loss in the

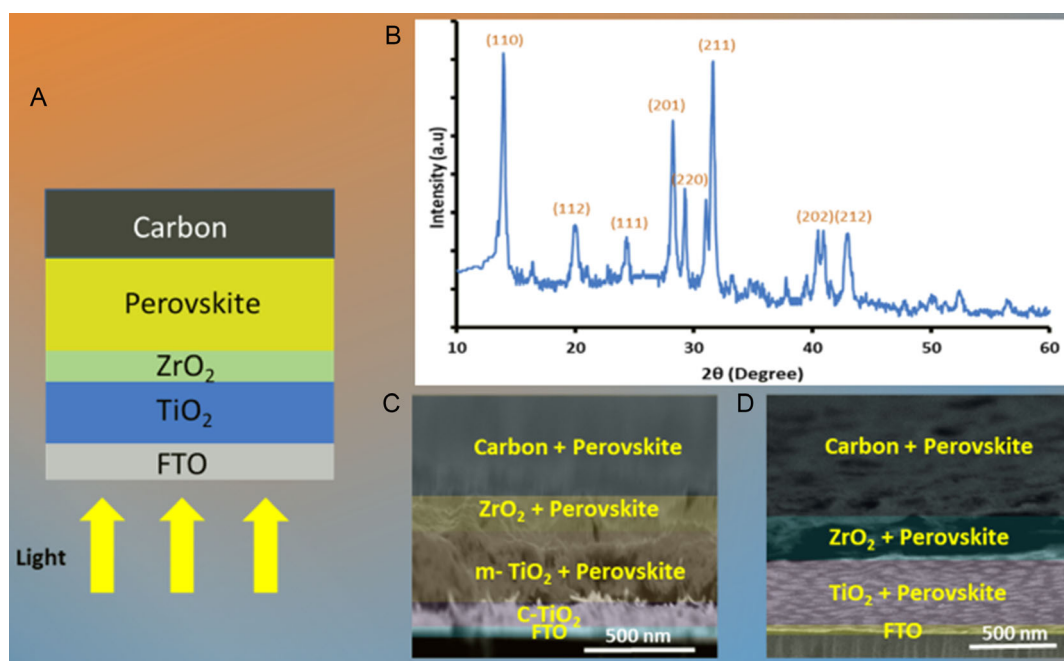


**Figure 1.** A) Device architecture used for the SCAPS simulation. B) XRD patterns of the halide perovskite with major peaks. C) Cross-sectional SEM image for the Type 1 C-PSC. D) Cross-sectional SEM image of the Type 2 C-PSC.

layer.<sup>[46]</sup> From the literature, it is found that the defect density value lower than  $10^{14} \text{ cm}^{-3}$  does not have a noteworthy impact on the PCE of HTL-free PSCs.<sup>[37]</sup> This is mainly because of the reduced charge carrier recombination, and with fewer defects, there are fewer recombination centers, allowing a larger number of charge carriers to contribute to the photocurrent.<sup>[37,38]</sup> Also, several literatures implicate that the lower defect density value does not hamper the PCE in the context of HTL-free C-PSCs.<sup>[37,38]</sup> Importantly, this study verifies that fact by showing the closeness of the experimental and theoretical performances of the devices, as demonstrated in the following sections. The fabrication techniques of the C-PSC influence the defect density values of the layer, and the defect density at times is much higher for the screen printing and dip coating techniques.<sup>[47]</sup>

Another factor influencing the simulation results is the sheet resistance of the carbon layer. As the carbon layer replaces metal electrodes, a carbon layer with higher resistance reduces the device's performance. The sheet resistance can be controlled by nanoparticle addition or through changes in the post-treatment methods.<sup>[29]</sup> However, uncontrolled perovskite crystallization and the higher resistance of the carbon layer hinder the C-PSC performance. On the other hand, increased work function enhances cell performance. In the simulation, the back contact work function values were varied from 4.2 to 5.2 eV, and they impacted the open-circuit voltage, fill factor, and efficiency of the C-PSC. The short-circuit current density remains almost stable with the back contact work function.<sup>[35]</sup>

### 3.3. Type 1: Lower Viscosity m-TiO<sub>2</sub> Pastes with Different Perovskite Film Thicknesses

#### 3.3.1. SCAPS Simulation Results for Type 1

Here, m-TiO<sub>2</sub> with lower viscosity has been used, where various rotation speeds in the spin coater give different thicknesses that align with the bandgap variations. As Table 2 indicates, three configurations used for the simulation and thickness of the m-TiO<sub>2</sub> film varied from 150 nm, 300 nm, and 450 nm, respectively. Although the perovskite infiltration technique was used for the device fabrication, perovskite layer thickness varied according

to the m-TiO<sub>2</sub> layer in the simulation. From the simulation results, the highest performance was achieved for the cell configuration with higher perovskite and m-TiO<sub>2</sub> film thickness. As this simulation was carried out under an ideal case, both the series and shunt resistance were not considered for all the cases.

Considering the results obtained from the simulation study, the sample 3 configuration depicts higher performance (displayed in Table 2). **Figure 2A** represents the *J-V* curve, and the *J*<sub>SC</sub> of  $24.275 \text{ mA cm}^{-2}$  was recorded for the sample with a higher absorber and the ETL layer thickness. As in **Figure 2B**, the EQE validates the data and sample 1 shows a maximum reflection around 400 nm, while others were near 370 nm. The EQE graph clearly indicates peak changes due to the bandgap difference among the ETL layers. The quantum efficiency indicates the solar cell's ability to incident photon carrier conversion at a given energy.<sup>[48,49]</sup> **Figure 2B** shows the quantum efficiency variation with the absorber and ETL layer thicknesses. It is clear that the lower absorber layer thickness diminishes the photon absorption process at higher wavelengths. Once the wavelength is more than 750 nm, the quantum efficiency is reduced to zero as the light is not absorbed due to the bandgap changes.<sup>[50,51]</sup>

#### 3.3.2. Results for Type 1

For the experimental verification, the cells with sample 3 configuration were fabricated using lower viscosity m-TiO<sub>2</sub>. While comparing with the simulation results, the current density was reduced from  $24.275$  to  $18.8 \text{ mA cm}^{-2}$  for the experimental champion device compared to simulation. The *J-V* curve depicted in **Figure 3A** and Table 2 points out the characteristics of the fabricated C-PSC. In order to understand the dual behavior of experimental and simulated PCE, EIS measurements were carried out. **Figure 3B** denotes the EIS Nyquist plot with the equivalent circuit diagram. A frequency from 1 to 10 MHz under 0.9 V bias was used as the parameter for the measurement. In the equivalent circuit diagram, *R*<sub>CT</sub> is the charge transfer resistance, which acts as the resistance between the perovskite and carbon interface.<sup>[52]</sup> The series resistance (*R*<sub>s</sub>) is the resistance across the

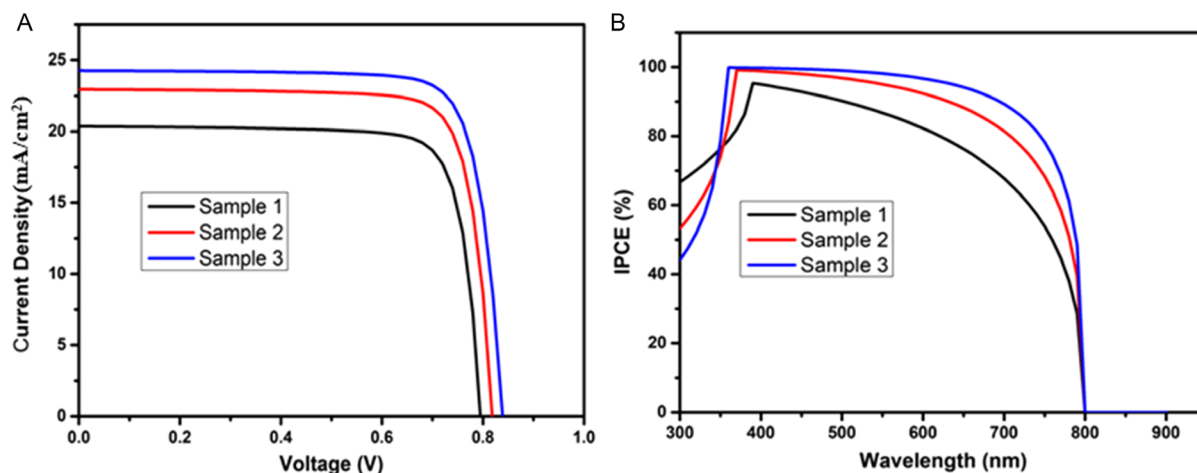


**Figure 2.** A) SCAPS-simulated *J-V* curves for three different configurations and B) corresponding EQE for the samples from the SCAPS simulation.

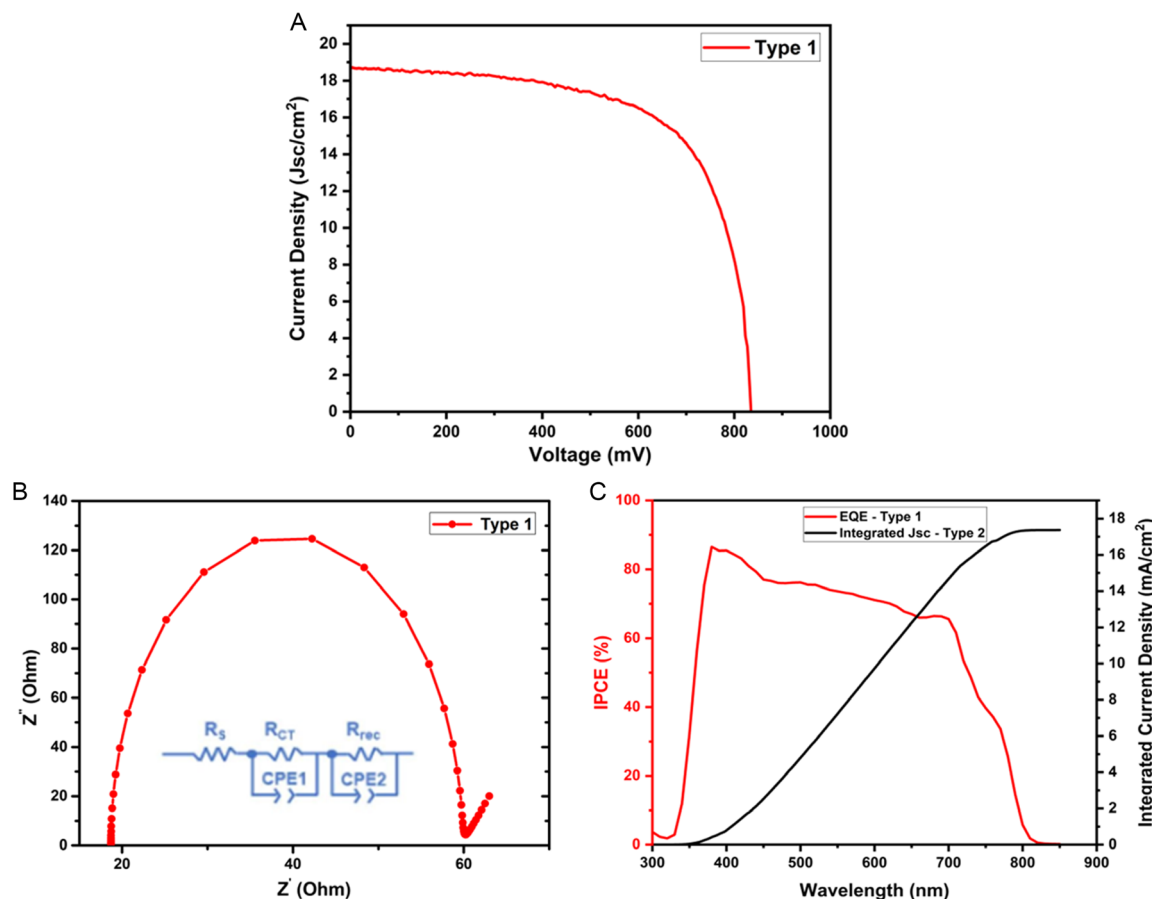


**Figure 3.** Experiment results of Type 1 C-PSCs. A) J–V curves of the fabricated champion device. B) EIS representation along with the electrical circuit diagram. C) EQE for the Type 1 C-PSC.

cell between the two terminals, FTO and carbon.<sup>[53]</sup>  $R_{rec}$  is the charge recombination resistance across the ETL and perovskite interface.<sup>[54]</sup> The C-PSC performance depends on the lower value of  $R_s$ , which implies better film quality via applied fabrication methods.<sup>[53,55]</sup> The impedance spectroscopy analysis of Type 1 C-PSC showed  $R_s$ ,  $R_{CT}$ , and  $R_{rec}$  values of 18.6, 40, and 922  $\Omega$ , respectively. Using the IPCE data, the EQE has been analyzed (Figure 3C) to evaluate the performance characteristics of the cell.

### 3.4. Type 2: Higher-Viscosity m-TiO<sub>2</sub> Pastes with Different Perovskite Film Thicknesses

#### 3.4.1. SCAPS Simulation Results for Type 2

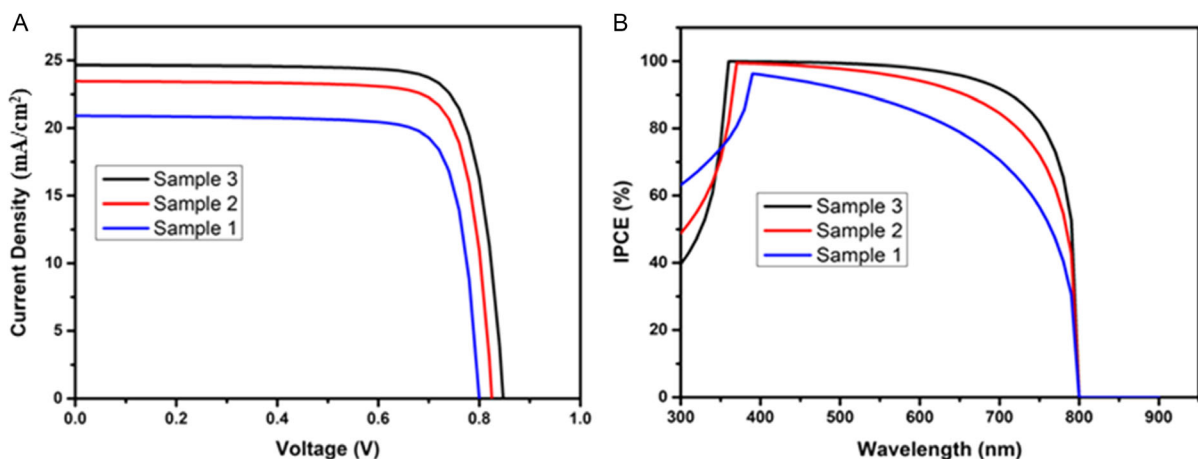
In this part, various configurations of C-PSC using the Type 2 m-TiO<sub>2</sub> layer or the higher viscous paste were analyzed with the help of SCAPS software. Except for the m-TiO<sub>2</sub> bandgap, ETL thickness, perovskite thickness, and all the other parameters for the simulation were made the same as in the previous case and illustrated in Table 1.

Figure 4A clearly indicates the difference in the current density and the open-circuit voltage for three different samples. For this simulation, the series and shunt resistance for the device

are not considered. However, the EQE analysis in Figure 4B stipulates the influence of bandgap variation, and it shows that the higher bandgap on sample 3 clears the way for wide range of reflection when compared to the other samples. The superior performing configuration consists of a perovskite layer with a higher thickness and enhanced bandgap, although after this point, the thickness did not affect much on the efficiency. While reducing the thicknesses and bandgap, there is a reduction in the PSC performance.

#### 3.4.2. Results for Type 2

The simulation understanding was taken into consideration for the experimental device fabrication. From the experiment results (Figure 5A and Table 3), it was observed that the C-PSC with the sample 3 configuration gives an efficiency of 12.2% with a fill factor of 68.70%. The current density decreased to 21.1 mA cm<sup>-2</sup> for the experimental device as compared to 24.66 mA cm<sup>-2</sup> during the simulation. Also, with the impedance spectroscopy analysis, the  $R_s$ ,  $R_{CT}$ , and  $R_{rec}$  are found to be 10.30, 16, and 1005, respectively. As shown in the Nyquist plot, Figure 5B, the series resistance is much lower when compared with the Type 1 C-PSC. This is mainly because of the increased thickness across the layers. One of the main reasons for the higher



**Figure 4.** A) SCAPS-simulated  $J-V$  curves for Type 2 configurations and B) corresponding EQE graph from SCAPS simulations.

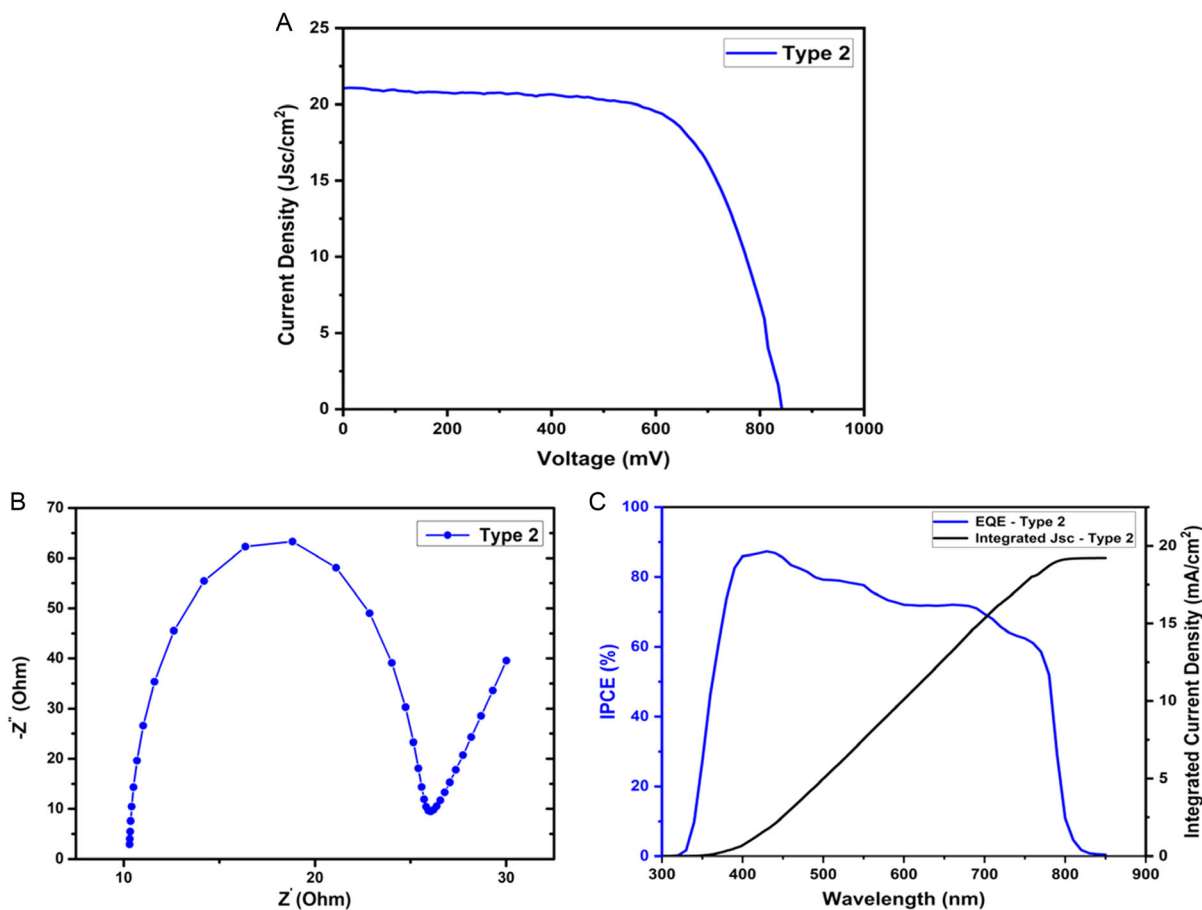


**Figure 5.** Experiment results for Type 2 fabricated C-PSC. A)  $J-V$  curves of the device. B) EIS performance of the device with the electrical circuit diagram. C) EQE performance of the Type 2 device.

efficiency of the Type 2 C-PSC is in relation to the effective thickness of the  $m\text{-TiO}_2$  and perovskite layers. Since the  $m\text{-TiO}_2$  layer can accommodate more perovskite as compared to the Type 1 configuration, a better cell performance was exhibited for

Type 2 C-PSC. In regard to the IPCE measurement, the EQE was calculated for the Type 2 cell. As Figure 5C indicates, nearly 90% of EQE was achieved around 400 nm and then reduced gradually.

**Table 3.** Various SCAPS simulation software configurations and experiment results for type 2.

No	Perovskite thickness [nm]	m-TiO <sub>2</sub> thickness [nm]	Rotation speed for m-TiO <sub>2</sub> layer [rpm]	m-TiO <sub>2</sub> bandgap [eV]	Simulation results	Efficiency [%]	V <sub>oc</sub> [V]	J <sub>sc</sub> [mA cm <sup>-2</sup> ]	FF
Sample 1	325	175	4000	3.2		13.53	0.799	20.91	80.10
Sample 2	500	350	3000	3.4		15.65	0.825	23.469	80.76
Sample 3	675	525	2000	3.5		16.81	0.848	24.66	80.35
Results									
Type 2 with sample 3 configuration		R <sub>S</sub> [Ω]	R <sub>CT</sub> [Ω]	R <sub>rec</sub> [Ω]		Efficiency [%]	V <sub>oc</sub> [mV]	J <sub>sc</sub> [mA cm <sup>-2</sup> ]	FF
		10.30	16	1005		12.20	0.842	21.1	68.70

### 3.5. Analysis of Dual Behavior of Experimental and Simulation Results

While considering the simulated performance of the rheology-varied TiO<sub>2</sub>-based C-PSC devices, the ideal conditions were applied, omitting the resistance factors. Meanwhile, the experimental devices showed the effect of resistances due to various interfacial contacts such as resistance of FTO glass and counter electrode ( $R_S$ ), resistance of the counter electrode/perovskite interface ( $R_{CT}$ ), and the resistance of the TiO<sub>2</sub>/perovskite interface ( $R_{rec}$ ), as shown in Figure 3B and 5B. These resistance factors significantly reduced the current density and fill factors of the experimental solar cells compared to simulated devices. Although the  $V_{OC}$  values are quite comparable for the simulated and experimental devices, the effect of reduced recombination is speculated to influence electron diffusion, which effectively reduces the current density of experimental champion C-PSCs. The lower the  $R_{CT}$  values, the better current and fill factors are expected for a device influencing the charge transport behavior.<sup>[56]</sup> Thus, in the real C-PSC devices, a significant deficiency of PCE was observed.

In order to validate the experiment results with the simulated performance, Type 1 and Type 2 C-PSC configurations have been included for simulation by adding both series and shunt resistance from experimental data. The series resistances were

obtained from impedance spectroscopy and the shunt resistances were gathered from the experimental dark current–voltage pattern. While considering the series and shunt resistance to the SCAPS simulation parameters, the efficiency has been reduced significantly. **Figure 6A,B** shows the current density and efficiency comparison of Type 1 and Type 2 C-PSCs in different cases. The T1E, T2E, T1SR, T2SR, T1S, and T2S represent Type 1 experiment results, Type 2 experiment results, Type 1 simulation results with resistance, Type 2 simulation results with resistance, Type 1 simulation results, and Type 2 simulation results, respectively. Both the T1SR and T2SR showed slightly better efficiency compared to their experimental counterparts. The simulation had the limitation of infiltrated perovskite devices as it can only predict the planar structure with a separate halide perovskite layer. The data obtained is shown in **Table 4**; additionally, it illustrates the significant difference in the current density and fill factor, although the efficiencies closely match with experimental results. The influential factors are the effect of charge transport efficiency and the difference in the charge carrier mobility across the coated layers. This could also include hysteresis effects, spatial nonuniformities in material properties or defects, and potential limitations or uncertainties in the experimental measurements. Comparing the experiment and simulation results, the coated layer quality affects the charge extraction and potentially reduces the fill factor. On the other side, the

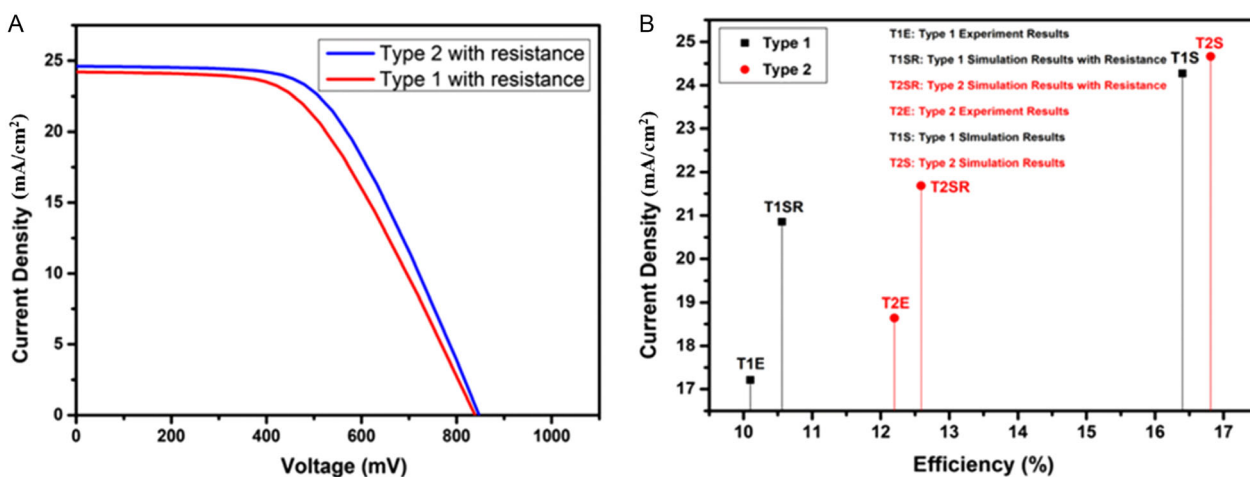


**Figure 6.** A) SCAPS simulation results with series and shunt resistance— $J$ – $V$  curves of the devices. B) Current density–efficiency details of various configurations.

**Table 4.** Series and shunt resistance from the experiment and the SCAPS simulation results with the resistance.

Devices	Series resistance [ $\Omega$ ]	Shunt resistance [ $\Omega$ ]	Efficiency	$V_{oc}$ [mV]	$J_{sc}$ [ $\text{mA cm}^{-2}$ ]	FF
Type 1	18.60	12867.57	10.56	839.09	24.21	51.97
Type 2	10.30	36913.73	12.59	848.41	24.62	55.36

drop-cast perovskite precursor on top of mesoporous carbon for C-PSC enhances the spreading of the ink by producing a uniform pattern of the film, which influences the fill factor.<sup>[57]</sup> Again, Figure 3C and 5C shows lesser IPCE coverage in the range of 450–780 nm, implying more pronounced surface defects for practical devices, which is supposed to influence the electron diffusion, and as a result, lower values of current densities were observed for experimental C-PSCs.<sup>[58]</sup> To sum up, although the experimental device pattern is a mesoporous infiltration type, the simulation results with all resistance factors exhibited a similar trend in PCE as the materials under consideration are the same, indicating this work's credibility and pathway to more inclusive future simulation–experimental conjugations using different directions of device fabrication. It is imperative to mention that the SCAPS simulation is unable to model key aspects of C-PSCs fabricated with the perovskite infiltration technique; the results may not fully reflect the actual behavior of the system, potentially leading to discrepancies between simulation predictions and experimental outcomes. However, by balancing the thickness of the perovskite layer during the experimental and theoretical study, as has been done in this work, the results can be interpreted as significantly accurate and reliable.

#### 4. Conclusion

In conclusion, we have demonstrated the rheology effect on HTL-free C-PSCs. Initial analyses were carried out through SCAPS simulations and then compared with the experimental results. The work showed differences in the thickness and bandgap of the ETL layer due to paste rheology and its effect on the PV performance. Two different types of rheology variation were considered, which were subdivided via thickness variations, and the simulation results showed better performance for the configuration with a higher bandgap and thickness of the  $\text{TiO}_2$  layer. However, despite the increase in efficiency according to thickness and bandgap, the fill factor values were reduced for both cases. Next, we analyzed the variation in fabricated C-PSC performance with the simulation results. As the simulation was conducted under ideal conditions without the effect of series and shunt resistance, the experimentally fabricated C-PSCs exhibited significantly lower performance. Nevertheless, the type 2 C-PSC device, fabricated with higher viscous paste, showed better performance experimentally due to the charge transport property at interfaces. The highest efficiency obtained for the higher viscous pastes was 16.81% during the simulation and 12.20% during practical fabrication. Although the conditions and fabrication mechanism for the layers coated with Type 1 and Type 2 pastes are the same, both the bandgap and thickness changed due to

rheological properties. Finally, this work highlights the importance of rheological studies for various materials used in C-PSC fabrication, which is essential for efficiency enhancement and the development of large-scale devices.

#### Acknowledgements

S.V. acknowledges the Engineering and Physical Sciences Research Council for the Ph.D. fellowship. This research was funded by Engineering and Physical Sciences Research Council, UK: PhD Fellowship and Engineering and Physical Sciences Research Council, UK: EP/T025875/1.

#### Conflict of Interest

The authors declare no conflict of interest.

#### Author Contributions

S.V., S.B. took care of conceptualization, investigation, methodology, data curation, analysis, writing the original draft, writing the review and editing, and visualization. T.K.M, J.H., S.S. took care of writing the review and editing, supervision, project administration, and funding acquisition.

#### Data Availability Statement

The data that support the findings of this study are available from the corresponding author upon reasonable request.

#### Keywords

hole transport layer-free perovskites, quantum efficiencies, rheologies, solar cell capacitance simulator (SCAPS) simulations

Received: October 31, 2023  
Revised: February 16, 2024  
Published online: February 27, 2024

- [1] H. Liu, C. Geng, P. Wei, H. Chen, S. Zheng, H. Wang, Y. Xie, *J. Alloys Compd.* **2022**, 912, 165123.
- [2] S. Bhandari, A. Roy, T. K. Mallick, S. Sundaram, *Mater. Lett.* **2020**, 268, 127568.
- [3] S. Bhandari, A. Roy, M. Sahidul Ali, T. K. Mallick, S. Sundaram, *Sci. Rep.* **2021**, 11, 23388.
- [4] A. Mattoni, A. Filippetti, C. Caddeo, S. Bhandari, T. K. Mallick, S. Sundaram, *J. Phys. Energy* **2023**, 5, 25006.
- [5] F. Meng, L. Gao, Y. Yan, J. Cao, N. Wang, T. Wang, T. Ma, *Carbon* **2019**, 145, 290.
- [6] U. Khan, T. Iqbal, M. Khan, R. Wu, *Sol. Energy* **2021**, 223, 346.
- [7] S.-H. Huang, C.-K. Guan, P.-H. Lee, H.-C. Huang, C.-F. Li, Y.-C. Huang, W.-F. Su, *Adv. Energy Mater.* **2020**, 37, 2001567.
- [8] O. Dupré, R. Vaillon, M. A. Green, *Sol. Energy Mater. Sol. Cells* **2015**, 140, 92.
- [9] N. Chatterji, A. Antony, P. R. Nair, *IEEE J. Photovolt.* **2019**, 9, 583.
- [10] S. Sheikh, A. Roy, S. Bhandari, T. K. Mallick, S. Sundaram, T. P. Sinha, *Mater. Lett.* **2020**, 276, 128220.
- [11] Best Research-Cell Efficiency Chart | Photovoltaic Research | NREL, <https://www.nrel.gov/pv/cell-efficiency.html> (accessed: July 2023).

- [12] F. Zhao, Y. Guo, P. Yang, J. Tao, J. Jiang, J. Chu, *J. Alloys Compd.* **2023**, 930, 167377.
- [13] G. Yue, D. Chen, P. Wang, J. Zhang, Z. Hu, Y. Zhu, *Electrochim. Acta* **2016**, 218, 84.
- [14] Y. Xiao, C. Wang, K. Kumar Kondamareddy, P. Liu, F. Qi, H. Zhang, S. Guo, X.-Z. Zhao, *J. Power Sources* **2019**, 422, 138.
- [15] R. Chen, Y. Feng, C. Zhang, M. Wang, L. Jing, C. Ma, J. Bian, Y. Shi, *J. Mater. Chem. C* **2020**, 8, 9262.
- [16] Z. Ku, Y. Rong, M. Xu, T. Liu, H. Han, *Sci. Rep.* **2013**, 3, 3132.
- [17] A. Mei, X. Li, L. Liu, Z. Ku, T. Liu, Y. Rong, M. Xu, M. Hu, J. Chen, Y. Yang, M. Grätzel, H. Han, *Science* **2014**, 345, 295.
- [18] Q.-Q. Chu, B. Ding, J. Peng, H. Shen, X. Li, Y. Liu, C.-X. Li, C.-J. Li, G.-J. Yang, T. P. White, K. R. Catchpole, *J. Mater. Sci. Technol.* **2019**, 35, 987.
- [19] H. Zhang, Y. Li, S. Tan, Z. Chen, K. Song, S. Huang, J. Shi, Y. Luo, D. Li, Q. Meng, *J. Colloid Interface Sci.* **2021**, 608, 3151.
- [20] Z. Huang, L. Li, H. Rao, Z. Pan, X. Zhong, *Sol. RRL* **2022**, 6, 2200145.
- [21] K. Wang, R. Yin, W. Sun, X. Huo, J. Liu, Y. Gao, T. You, P. Yin, *Sol. RRL* **2022**, 6, 2100647.
- [22] X. Chen, Y. Xia, Q. Huang, Z. Li, A. Mei, Y. Hu, T. Wang, R. Cheacharoen, Y. Rong, H. Han, *Adv. Energy Mater.* **2021**, 11, 2100292.
- [23] X. Chen, Y. Xia, Z. Zheng, X. Xiao, C. Ling, M. Xia, Y. Hu, A. Mei, R. Cheacharoen, Y. Rong, H. Han, *Chem. Mater.* **2022**, 34, 728.
- [24] F. Yang, L. Dong, D. Jang, B. Saparov, K. C. Tam, K. Zhang, N. Li, C. J. Brabec, H. J. Egelhaaf, *Adv. Energy Mater.* **2021**, 11, 2101219.
- [25] J. Du, C. Qiu, S. Li, W. Zhang, W. Zhang, Y. Wang, Z. Qiu, Q. Wang, K. Yang, A. Mei, Y. Rong, Y. Hu, H. Han, *Adv. Energy Mater.* **2022**, 12, 2102229.
- [26] L. Calió, S. Kazim, M. Grätzel, S. Ahmad, *Angew. Chem. Int. Ed.* **2016**, 55, 14522.
- [27] Q. Duan, J. Ji, X. Hong, Y. Fu, C. Wang, K. Zhou, X. Liu, H. Yang, Z.-Y. Wang, *Sol. Energy* **2020**, 263, 111885.
- [28] S. Li, Y. Li, Y. Li, F. Deng, X. Sun, X. Tao, *J. Sol. Energy Mater. Sol. Cells* **2023**, 257, 112391.
- [29] S. Bhandari, S. Valsalakumar, Y. Chanchangi, P. Selvaraj, T. K. Mallick, *RSC Adv.* **2023**, 13, 7380.
- [30] P. Liu, G. Tang, F. Yan, *Sol. RRL* **2022**, 6, 2100683.
- [31] B. Parida, A. Singh, A. K. Kalathil Soopy, S. Sangaraju, M. Sundaray, S. Mishra, S. Liu, A. Najar, *Adv. Sci.* **2022**, 9, 2200308.
- [32] A. Giuri, E. Saleh, A. Listorti, S. Colella, A. Rizzo, C. Tuck, C. E. Corcione, *Nanomaterials* **2019**, 9, 582.
- [33] S. X. Zheng, H. S. Chen, *Prog. Org. Coat.* **2023**, 177, 107403.
- [34] Q. J. Wang, Y. Chung, *Encyclopedia of Tribology*, American Institute of Physics **2013**.
- [35] M.-R. Ahmadian-Yazdi, A. Rahimzadeh, Z. Chouqi, Y. Miao, M. Eslamian, *AIP Adv.* **2018**, 8, 25109.
- [36] G. Tong, D. Y. Son, L. K. Ono, Y. Liu, Y. Hu, H. Zhang, A. Jamshaid, L. Qiu, Z. Liu, Y. Qi, *Adv. Energy Mater.* **2021**, 11, 2003712.
- [37] L. Lin, P. Li, L. Jiang, Z. Kang, Q. Yan, H. Xiong, S. Lien, P. Zhang, Y. Qiu, *Sol. Energy* **2021**, 215, 328.
- [38] E. Raza, Z. Ahmad, M. Asif, F. Aziz, K. Riaz, M. Q. Mehmood, J. Bhadra, N. J. Al-Thani, *Opt. Mater.* **2022**, 125, 112075.
- [39] S. Valsalakumar, A. Roy, T. K. Mallick, J. Hinshelwood, S. Sundaram, *Mater. Lett.* **2023**, 337, 133960.
- [40] M. Burgelman, P. Nollet, S. Degraeve, *Thin Solid Films* **2000**, 361, 527.
- [41] W. R. McGovern, P. Schmutz, R. G. Buchheit, A. Mosleh, M. A. Alher, L. Cousar, K. Ui, S. Kobayashi, P. Srivastava, S. Rai, P. Lohia, D. K. Dwivedi, H. Qasem, A. Umar, S. Akbar, H. Algadi, S. Baskoutas, *Phys. Scr.* **2022**, 97, 125004.
- [42] M. Khalid Hossain, M. Humaun Kabir Rubel, G. F. Ishraque Toki, I. Alam, M. Ferdous Rahman, H. Bencherif, *ACS Omega* **2022**, 7, 295.
- [43] M. K. A. Mohammed, A. K. Al-Mousoi, S. M. Majeed, S. Singh, A. Kumar, R. Pandey, J. Madan, D. S. Ahmed, D. Dastan, *Energy Fuels* **2022**, 36, 13187.
- [44] S. G. Hashmi, D. Martineau, M. I. Dar, T. T. T. Myllymäki, T. Sarikka, V. Ulla, S. M. Zakeeruddin, M. Grätzel, *J. Mater. Chem. A* **2017**, 5, 12060.
- [45] Y. Lei, Y. Li, Z. Jin, *Energy Rev.* **2022**, 1, 100003.
- [46] M. Jamal, S. Shahahmadi, M. Aizat Abdul Wadi, P. Chelvanathan, N. Asim, H. Misran, M. Hossain, N. Amin, K. Sopian, M. Akhtaruzzaman, *Optik* **2019**, 182, 1204.
- [47] S. Tariq Jan, M. Noman, *Sol. Energy* **2022**, 237, 29.
- [48] S. Ravishankar, C. Aranda, P. P. Boix, J. A. Anta, J. Bisquert, G. Garcia-Belmonte, *J. Phys. Chem. Lett.* **2018**, 9, 3099.
- [49] L. V. Mercaldo, E. Bobeico, A. De Maria, M. Della Noce, M. Ferrara, L. Lancellotti, A. Romano, G. V. Sannino, G. Nasti, A. Abate, P. Delli Veneri, *Energy Technol.* **2022**, 10, 2200748.
- [50] S. Weng, A. Tamang, A. Salles, H. Fujiwara, M. Nakamura, Y. Zhang, D. Knipp, *ACS Appl. Mater. Interfaces* **2021**, 13, 39230.
- [51] W. Tress, N. Marinova, O. Inganäs, M. K. Nazeeruddin, S. M. Zakeeruddin, M. Graetzel, *Adv. Energy Mater.* **2015**, 5, 1400812.
- [52] P. Yadav, M. H. Alotaibi, N. Arora, M. I. Dar, S. M. Zakeeruddin, M. Grätzel, P. Yadav, N. Arora, M. I. Dar, S. M. Zakeeruddin, M. Grätzel, M. H. Alotaibi, *Adv. Funct. Mater.* **2018**, 28, 1706073.
- [53] N. Mundhaas, Z. J. Yu, K. A. Bush, H.-P. Wang, J. Häusele, S. Kavadiya, M. D. McGehee, Z. C. Holman, N. Mundhaas, Z. J. Yu, J. Häusele, S. Kavadiya, Z. C. Holman, K. A. Bush, H. Wang, M. D. McGehee, *Sol. RRL* **2019**, 3, 1800378.
- [54] A. D. Sheikh, R. Munir, M. A. Haque, A. Bera, W. Hu, P. Shaikh, A. Amassian, T. Wu, *ACS Appl. Mater. Interfaces* **2017**, 9, 35018.
- [55] J. Zhang, E. J. Juárez-Pérez, I. Mora-Seró, S. Seró, B. Viana, T. Pauporté, P. Pauporté, *J. Mater. Chem. A* **2015**, 3, 4909.
- [56] S. Bhandari, A. Roy, T. K. Mallick, S. Sundaram, *J. Chem. Eng.* **2022**, 446, 137378.
- [57] A. Listorti, E. J. Juárez-Pérez, C. Frontera, V. Roiati, L. Garcia-Andrade, S. Colella, A. Rizzo, P. Ortiz, I. Mora-Sero, *J. Phys. Chem. Lett.* **2015**, 6, 1628.
- [58] L. Zhu, Z. Shao, J. Ye, X. Zhang, X. Pan, S. Dai, *Chem. Commun.* **2016**, 52, 970.
- [59] H.-J. Du, W.-C. Wang, Y.-F. Gu, *Chin. Phys. B* **2017**, 26, 028803.
- [60] H. Yuan, Z. Zhang, T. Guo, L. Yu, Z. Deng, R. Zhao, J. Zhang, Y. Zhu, *J. Alloys Compd.* **2021**, 876, 160140.
- [61] P. Schulz, E. Edri, S. Kirmayer, G. Hodes, D. Cahen, A. Kahn, *Energy Environ. Sci.* **2014**, 7, 1377.
- [62] G. Giorgi, J.-I. Fujisawa, H. Segawa, K. Yamashita, *J. Phys. Chem. Lett.* **2023**, 15, 56.
- [63] C. Wehrenfennig, G. E. Eperon, M. B. Johnston, H. J. Snaith, L. M. Herz, *Adv. Mater.* **2014**, 26, 1584.